

Versatile Top-Down Patterning of 3D, 2D and 0D Perovskites for On-Chip Integration

Federico Fabrizio^{1,2,°}, Saeed Goudarzi^{2,°}, Sana Khan^{1,2}, Tauheed Mohammad¹, Liudmila Starodubtceva², Piotr J. Cegielski¹, Gerhard Müller-Newen³, Surendra B. Anantharaman^{1,4}, Maryam Mohammadi^{1,}, Max C. Lemme^{1,2,*}*

¹ AMO GmbH, Otto-Blumenthal-Straße 25, Aachen, Germany.

² Chair of Electronic Devices, RWTH Aachen University, Otto-Blumenthal-Straße 25, Aachen, Germany.

³ Institute of Biochemistry and Molecular Biology, Uniklinik RWTH Aachen, Pauwelsstrasse 30, Aachen, Germany.

⁴ Low-dimensional Semiconductors (LDS) Lab, Indian Institute of Technology Madras, Chennai, Tamil Nadu, India.

[°]These authors contributed equally.

*Corresponding Authors – mohammadi@amo.de, lemme@amo.de

KEYWORDS: Metal-halide perovskites, on-chip integration, top-down patterning, photolithography, reactive ion etching

Abstract

Metal-halide perovskites (MHPs) have exciting optoelectronic properties and are under investigation for various applications, such as photovoltaics, light-emitting diodes, and lasers. An essential step toward exploiting the full potential of this class of materials is their large-scale, on-chip integration with high-resolution, top-down patterning. The development of such patterning methods for perovskite films is challenging because of their ionic behavior and adverse reactions with the solvents used in standard lithography processes. Here, we

introduce a versatile and precise method comprising photolithography and reactive ion etching (RIE) processes that can be tuned to accommodate different perovskite compositions and morphologies, including 3D, quasi-2D, and quasi-0D structures. Our method utilizes conventional photoresists at reduced temperatures to create micron-sized features down to 1 μm , providing high reproducibility from chip to chip. The patterning technique is validated through atomic force microscopy (AFM), X-ray diffraction (XRD), optical spectroscopy, and scanning electron microscopy (SEM). It enables the scalable and high-throughput on-chip monolithic integration of MHPs.

Introduction

Metal-halide perovskites (MHPs) are a class of ionic semiconductors known for their outstanding optoelectronic properties, including charge carrier diffusion lengths exceeding $1\ \mu\text{m}^{[1-4]}$ and a direct bandgap^[5-7]. These properties have spawned substantial research in various fields, such as photovoltaics^[8-10], photonics^[11-14], and optoelectronics^[15-19]. Furthermore, the optoelectronic properties of MHPs, including their bandgap, binding energy, and charge carrier mobility, depend on both their composition and dimensionality^[5,20]. The engineering of the composition of MHPs is facilitated by their rich chemistry, which provides opportunities for tuning their electronic and optical properties^[21,22]. Additionally, the dimensionality of MHPs can be altered from three-dimensional (3D)^[23] to two-dimensional (2D)^[24], one-dimensional (1D)^[25], and zero-dimensional (0D)^[26].

Technologically, their simple, low-temperature solution-based deposition processes^[27] are beneficial for upscaling production once the relevant technology readiness levels are achieved. However, integrated on-chip applications in optoelectronics and photonics, such as displays or light-emitting diodes (LEDs)^[28-30], require compatibility with the perovskites' limited thermal budgets and complex semiconductor manufacturing processes^[31-34]. One of the key processes for such integration is the patterning of perovskite materials^[35,36]. The industry's standard and preferred technique combines top-down photolithography and reactive ion etching (RIE) because of its high resolution, precision, reliability, selectivity, and good cost-performance trade-off. However, traditional photolithography involves wet chemical processing in polar solvents and deionized water, which damages or resolves highly ionic crystals such as perovskites^[37,38]. This chemical instability and sensitivity to polar and protic solvents^[39], which are present in photoresist spin-coating processes, lead to degradation or alteration of the intrinsic properties of the perovskite. Several alternative methods have been developed, such

as nanoimprint patterning^[40–42], fluorinated resists^[43], gas-assisted focused ion beam etching^[44], inkjet printing^[45], laser writing^[46,47] and wettability-assisted photolithography (WAP) processes^[48,49]. However, these methods do not generally meet the industry's needs for high-speed production on a wafer scale and accurate and consistent features.

Here, we demonstrate a precise and reproducible method for the top-down patterning of perovskite films with micrometer resolution on the basis of standard semiconductor equipment and processes. The method can be tailored for various perovskite types and morphologies, including 3D and low-dimensional (quasi-2D and 0D) structures. We use a double-stack resist composed of polymethyl methacrylate (PMMA) and AZ MIR 701, a commercial positive photoresist^[50]. The PMMA prevents direct contact between the perovskite and photoresists^[51], whereas AZ MIR 701 facilitates a standard lithography process. We subsequently employ RIE to etch the perovskites while avoiding oxygen plasma, which also damages the perovskites^[39].

Methods

Motivated by earlier works on perovskite-compatible photolithography methods^[28,39,52], we devised a new strategy that integrates two resists and non-oxidative reactive gases into a singular workflow. In the following, we introduce the method and demonstrate its application to 3D cesium lead bromide (CsPbBr_3) and methylammonium lead iodide (MAPbI_3), quasi-2D ($\text{PEA}_2(\text{MAPbBr}_3)_{n-1}\text{PbBr}_4$) and 0D formamidinium lead bromide (FAPbBr_3) perovskites.

The different perovskite thin films were spin-coated onto a Si/SiO₂ substrate (see Experimental Section for more details). A 200 nm encapsulation layer (PMMA) was deposited on top of the perovskite layer via spin-coating at 4000 rpm for 60 seconds and baking at 80°C for 10 minutes.

This layer acted as a spacer layer and protected the perovskite material from the photoresist.

Then, the AZ MIR 701 photoresist was spin-coated on top of the samples at 3000 rpm for 60 s

and soft-baked at 95°C for 90 s, after which the samples were exposed to ultraviolet (UV) light for 25 s via a contact lithography mask aligner (EVG 420) system. The patterns were developed in MF26A developer for 35 s followed by rinsing for 7 s with deionized water. Then, the samples were etched via a PlasmaLab System 100 inductively coupled plasma (ICP)-RIE tool (Oxford Instruments). All inorganic 3D metal halides, quasi-2D perovskites, and nanocrystalline thin films were etched with radicals from HBr and BCl₃ gases with different gas flows. The hybrid organic-inorganic perovskites were etched with radicals from CF₄, Cl₂ and He gas. Since the metal halide perovskites are sensitive to high temperatures, the etching processes were performed in a step and repeated fashion with one cycle of etching followed by a waiting cycle for two minutes to reduce the substrate temperatures. The etching rate of CsPbBr₃ was 100 nm/min, and the selectivity over SiO₂ was 3.6, whereas for MAPbI₃, the values were 90 nm/min and 2.7. The etch rate and selectivity over SiO₂ for the quasi-2D perovskite were 95 nm/min and 3.4, and the values for the 0D FAPbBr₃ were 92 nm/min and 2.8. Finally, the photoresist stack was removed by dissolving the PMMA encapsulation layer in the non-polar solvent toluene at 80°C for 1 hour to ensure complete dissolution of the PMMA. A schematic of the process is shown in Figure 1. The process yielded perovskite features as small as 1 μm, which is the smallest resolution achievable with our contact lithography system (Figures 1b and c).

Results

1. Photolithographic patterning of three-dimensional MHPs

We investigated our process with the 3D perovskites CsPbBr₃ and MAPbI₃ because they are the most studied and technologically mature metal halide perovskites.

1.1. All-inorganic perovskite (CsPbBr₃)

Figures 2a and b show atomic force microscopy (AFM) images of the surface topology of the CsPbBr₃ thin film before and after etching. The bright areas with greater heights are attributed to the material's secondary phases of CsPb₂Br₅ and Cs₄PbBr₆, as evidenced by X-ray diffraction (XRD) measurements (Figure 2c), corroborating previous findings^[13]. The root mean square (RMS) roughness was 14.92 ± 1.57 nm, which increased to 24.09 ± 1.21 nm after the etching process. We also observed an increase in the average grain size from approximately 65 nm after spin coating to 200 nm after stripping the double-stack resist (Supporting Information (SI) Figures S1a and b) and an increase in the number of pinholes in the film. This suggests some degree of recrystallization during the etching process, despite tailoring the etching recipe to limit process-induced heating.

The XRD data in Figure 2c show no significant differences in the crystalline phases before and after etching. The spectra show distinct high-intensity peaks at 15.21° , 21.49° , 26.37° , 30.69° , 34.46° , and 37.90° , corresponding to the (100), (110), (111), (200), ($\bar{2}10$), and ($\bar{2}11$) crystallographic planes, respectively, characteristic of monoclinic CsPbBr₃ (reference code: 00-018-0364)^[54]. Additional peaks were observed at 12.63° , 22.41° , 25.42° , 27.51° , and 28.63° , indicative of the presence of the (012), (300), (024), (131), and (214) crystallographic planes, respectively, associated with the rhombohedral Cs₄PbBr₆ phase (reference code: 01-073-2478)^[55]. Furthermore, some peaks attributed to the (002), (024), (131), and (241) planes of the CsPb₂Br₅ phase were observed, supporting the results of the AFM analysis^[56,57].

The patterned perovskites were optically characterized through ultraviolet–visible (UV-Vis) absorption and photoluminescence (PL) spectroscopy. The absorption edges before and after the etching process were very similar, approximately 516 nm and 517 nm, respectively. The photoluminescence peaks remained at 521 nm before and after the etching process, with full widths at half maximum (FWHM) of 15.1 nm and 14.9 nm, respectively (see individual spectra in Figure 2d). PL emission maps taken over large scan areas of 25 μm \times 25 μm confirmed this result. They are shown in Figures 2e and f, where the color scale indicates the peak position wavelength. The FWHM of the PL spectra also did not change before and after the etching process in the same scanning areas (SI Figures S1c and d). Moreover, no differences can be discerned in the PL spectra between the center and edges of the etched structures (SI Figure S1e).

Figure 2g shows a cross-sectional SEM image of the etched CsPbBr₃ sidewall with an angle of approximately 85°. Furthermore, the top-view SEM image, profilometer measurement and optical microscope image after etching in SI Figures S1f, g and h display low edge roughness and well-defined structures. Figure 2h shows a confocal microscopy image of typical patterns that can be achieved with CsPbBr₃, with the characteristic luminescence wavelength in the green range of the spectrum.

1.2. Organic-inorganic hybrid perovskite (MAPbI₃)

We further investigated our etching method with the less stable organometallic halide perovskite MAPbI₃, following the same fabrication scheme illustrated in Figure 1.

The morphology of the MAPbI₃ thin film before and after etching was examined via AFM (Figures 3a and b). The RMS roughness slightly increased from 6.20 \pm 1.99 nm to 7.06 \pm 1.08 nm after etching. In contrast to CsPbBr₃, there were no noticeable changes in the grain size of MAPbI₃. (from 146.85 \pm 70.94 nm to 158.64 \pm 81.97 nm, SI Figures S2a and b).

The XRD spectra of MAPbI₃ before and after etching have dominant peaks at 14.09°, 19.93°, 23.54°, 24.52°, 28.45°, 31.85°, and 34.9°, corresponding to the (110), (200), (211), (202), (220), (310) and (312) crystallographic planes of the tetragonal phase of MAPbI₃, respectively [58,59]. A minor peak attributed to the PbI₂ phase is also evident at 12.7°[58]. After etching, an additional peak occurred at 15.1°, indicating a different material composition at the edges of the patterned areas. Confocal microscopy images of these areas showed blue and green emissions all over the edges (SI Figures S2c, d, and e), which can be attributed to halide exchange with chlorine radicals from the etch plasma, resulting in the formation of MAPbI_{3-x}Cl_x (0<X≤3) [58]. This is enabled by the low crystal formation energy of organic-inorganic hybrid metal halides, facilitating the chlorine ion diffusion.

UV-Vis absorption and PL spectra of the patterned MAPbI₃ structures show absorption edges and photoluminescent peaks at 748 nm and 768 nm, respectively, and no significant wavelength shifts were observed before and after etching in the sample center (Figure 3d). The FWHM values of 37.4 nm and 37.2 nm before and after etching, respectively, are comparable. However, the region close to the edge of the MAPbI₃ shows a blueshift of approximately 7 nm in the PL peak position (SI Figure S2f). This can be explained by decreased average grain sizes at the edge of the etched structure (SI Figure S2g), which also contributed to an enhanced PL intensity (inset of SI Figure S2f). Similar effects were reported previously for perovskite thin films^[28,61] and single crystals^[62]. PL maps (Figures 3e and f) and an analysis of the FWHM (SI Figures S2h and i) over an area of 25 μm × 25 μm in the center of the samples demonstrate the optical stability of MAPbI₃ towards the patterning process.

Figure 3g shows a cross-sectional SEM image of the MAPbI₃ sidewall with an angle of approximately 80°. Moreover, top-view SEM image, optical microscope image, and profilometer measurement after etching (SI Figure S2l, m, and n) demonstrate the structured

MAPbI₃ with a lateral size of 85 μm by 65 μm and a height of 250 nm. Figure 3h shows a confocal microscopy image of typical patterns that can be achieved with MAPbI₃, with the characteristic luminescence wavelength in the red range of the spectrum.

2. Photolithographic patterning of low-dimensional MHPs

2.1. Quasi-two-dimensional perovskites (PEA₂(MAPbBr₃)_{n-1}PbBr₄)

Next, we demonstrated the suitability of the patterning technique in Figure 1 for the fabrication of high-resolution quasi-2D perovskite arrays.

AFM images in Figures 4a and b show that the morphology of the perovskites was retained after the process. The roughness of the film decreased from 57.51 ± 8.95 nm to 50.66 ± 15.84 nm, indicating a smoothing effect through the etching process.

The XRD spectra in Figure 4c remained unchanged before and after patterning and show four sharp peaks at 5.07°, 14.95°, 21.38°, and 30.20°, corresponding to the (002), (100), (110), and (200) crystal planes of the quasi-2D perovskites, respectively^[63]. The low-angle diffraction peak below 5° can be attributed to typical reflections from the layered structure^[64].

The UV–Vis and PL spectra in Figure 4d show absorption edges and photoluminescence peaks at 517 nm and 528 nm, respectively, and no significant peak position shift before and after etching. This is uniform across the sample, as illustrated in the PL emission maps, with only a slight variability of 2 nm in the emission wavelength over an area of 25 μm x 25 μm (Figures 4e and f). An average reduction of approximately 2 nm in the FWHM was observed in area scans (SI Figures S3a and b). The PL spectra showed no significant differences in emission wavelengths between the center and the edge of the structures (SI Figure S3c).

The cross-sectional SEM image in Figure 4g shows well-defined structures after the etching process, with a sidewall angle of approximately 85°. The confocal microscopy image in Figure 4h confirms the successful etching of the quasi-2D perovskite with its green emission,

with no residual perovskite in the etched area. In addition, the quality of the etched $\text{PEA}_2(\text{MAPbBr}_3)_{n-1}\text{PbBr}_4$ structures is shown in SI Figures S3d, e, and f. The top-view SEM image, optical microscope image, and profilometer measurement after etching illustrate the structured $\text{PEA}_2(\text{MAPbBr}_3)_{n-1}\text{PbBr}_4$ with a lateral size of $85\ \mu\text{m}$ by $65\ \mu\text{m}$ and a height of $290\ \text{nm}$. These data demonstrate that our technology is applicable to quasi-2D perovskites.

2.2. Zero-dimensional perovskites (FAPbBr₃)

Finally, we applied our micropatterning technique to thin films of colloidal FAPbBr₃ perovskite nanocrystals (NCs).

The surface roughness of the NC layers was assessed by AFM before and after the etching process (Figures 5a and b), the film roughness decreased from $6.72 \pm 0.32\ \text{nm}$ to $5.21 \pm 0.83\ \text{nm}$.

The XRD spectra taken before and after patterning were not significantly affected (Figure 5c), with four characteristic peaks of the cubic structure of FAPbBr₃ that correspond to the (100), (110), (200) and (210) crystal planes^[65,66]. The Scherrer equation ($D = \frac{K\lambda}{\beta \cos\theta}$) can be used to measure the size of the nanocrystal. It revealed no significant reduction in the size: $9.66\ \text{nm}$ and $9.12\ \text{nm}$ before and after etching, respectively.

The UV-Vis and PL spectra of the NCs exhibited differences in their absorption edges and photoluminescence peaks before and after the etching process. As illustrated in Figure 5d, both spectra show a blueshift of approximately $8\ \text{nm}$ after the etching process. The absorption edge before the nanofabrication process was located at $518\ \text{nm}$, whereas it was $510\ \text{nm}$ after the etching process. A similar trend was observed for the PL peak position, which moved from $521\ \text{nm}$ to $513\ \text{nm}$. This is confirmed in Figures 5e and f, where an average blueshift of the PL peak position of $8\ \text{nm}$ was extracted from the $25\ \mu\text{m} \times 25\ \mu\text{m}$ area scan. The FWHM before and after etching remained very similar at $19.47\ \text{nm}$ and $19.18\ \text{nm}$, respectively. This was

confirmed in the respective area maps (SI Figures S4a and S4b). There were also no noticeable differences in the emission peak positions between the center and edge of the etched structure (SI Figure S4c).

The cross-sectional SEM image in Figure 5g shows well-defined structures after the etching process, with an angle of approximately 80° . The structured FAPbBr_3 NCs exhibit uniform green photoluminescence, as illustrated by the confocal fluorescence microscope image in Figure 5h. Well-defined regular patterns of NC-based thin films with a thickness of approximately 230 nm (see optical microscope images and surface profile data in Figures S4d, e and f). A comparison of the two profilometer line scans before (Figure S4g) and after (Figure S4f) the nanofabrication process revealed a height difference of approximately 20 nm. We attribute this result to the bonding of carboxyl (COOH) groups in PMMA with the unpassivated ionic lead (Pb^{2+}) on the surface^[67], resulting in the lifting of some surface layers of the NCs thin film during the PMMA removal. This could also account for the roughness reduction after the patterning process observed by AFM.

Conclusions

We developed a top-down patterning technique for Metal-halide perovskites based on conventional lithography and reactive ion etching. We demonstrated the method on organic-inorganic hybrids and all-inorganic compounds with different dimensionalities (3D, 2D, and 0D). The technique was evaluated via AFM, XRD, optical spectroscopy, and SEM, confirming that the phase and optical properties of the perovskites were not affected by the patterning process, except at the edges of the patterned organic-inorganic metal halide perovskite. The organometal halide perovskite MAPbI_3 showed local halide exchange at the edges of the patterned area with the etching gas ions, which can be explained by its intrinsic soft lattice crystal structure. The developed microstructuring technique showed reproducible results with

a resolution down to 1 μm . It is applicable on the wafer scale and can achieve smaller dimensions with higher-resolution photolithography tools. Therefore, it can be used to monolithically integrate different types of metal-halide perovskites on chip with industry-standard processes. Our technology enables flexible device engineering and can accelerate the research and development of perovskite-based optoelectronics, electronics and energy harvesting applications.

Methods

Substrates: Si/SiO₂ chips were diced and cleaned from the protective polymer layer by sonication in acetone and isopropanol, followed by 10 minutes of oxygen plasma cleaning in an RF plasma reactor. The chips were subsequently transferred into a nitrogen-filled glove box for the perovskite deposition processes.

Perovskite Deposition:

All-inorganic perovskite thin films, namely, CsBr (> 99.0%, TCI) and PbBr₂ (≥ 98%, Sigma Aldrich), were combined at a 1:1.7 molar ratio of 14% by weight, dissolved in dimethylsulfoxide (DMSO, anhydrous, ≥ 99.9%), and then left overnight at 60°C on a hot plate. The precursor solution was subsequently filtered via 0.20 μm pore size polytetrafluoroethylene (PTFE) filters. Finally, 80 μl of the precursor solution was spin-coated onto the cleaned Si/SiO₂ substrates at 2000 rpm for 40 seconds, followed by a thermal annealing process at 80°C for 10 minutes.

Organic–inorganic hybrid perovskite thin films: The MAPbI₃ perovskite solution was prepared with 1 M methylammonium (CH₃NH₃I, TCI), lead iodide (PbI₂, 99.999%, Sigma Aldrich), and dimethyl sulfoxide (DMSO, anhydrous, ≥ 99.9%). These compounds were dissolved in 1 ml of dimethylformamide (DMF, anhydrous, 99.8%) and heated to 60°C for 1 hour while stirring. The resulting solution was then filtered through a 0.20 μm pore size PTFE filter and spin-coated onto the cleaned Si/SiO₂ substrates at 6000 rpm for 30 seconds. Six seconds after the spin started, 300 μl of chlorobenzene (anhydrous, 99.8%) was added. The resulting film underwent a two-step annealing process (45°C for 5 minutes followed by 100°C for 10 minutes) to complete the conversion of the precursors into the MAPbI₃ perovskite layer.

Quasi-2D perovskite thin films: PEA₂(MAPbBr₃)_{n-1}PbBr₄ quasi-2D perovskite thin films were deposited via the spin coating technique. First, the perovskite solution was prepared by dissolving 0.4 mmol of methylammonium bromide (MABr, Sigma Aldrich), 0.6 mmol lead

bromide (PbBr_2 , TCI), 0.4 mmol phenylethylammonium bromide (PEABr, Sigma Aldrich), and 0.06 mmol methylammonium chloride (MACl, TCI) in 1 ml of DMSO. The prepared solution was stirred overnight at 60°C. 80 μl of filtered perovskite solution was spin-coated at 3000 rpm for 2 minutes and then annealed at 100°C for 30 minutes.

Perovskite nanocrystalline thin films: FAPbBr₃ NCs were synthesized via a hot-injection method at the Kovalenko laboratory via a previously published protocol^[68]. The NC solution was dissolved in cyclohexane at a concentration of approximately 20 mg/ml. The solution was spin-coated at 2400 rpm for 30 seconds and then at 10000 rpm for 1 second.

Photoluminescence Mapping: Photoluminescence mapping was performed via a WITec confocal Raman microscope (model alpha300R). The samples were scanned with a 457 nm CW laser at 1 μW power. The measurements were taken at room temperature under ambient conditions.

UV-Vis absorption spectroscopy: The absorption spectrum of each sample before and after etching was recorded via ultraviolet-visible light spectrophotometry (PerkinElmer Lambda 1050) in the wavelength range of 300 to 800 nm.

AFM, XRD, and SEM inspection: AFM images were taken from each sample before and after etching via an atomic force microscope (Bruker Dimension Icon) in tapping mode. XRD with filtered Cu-K α radiation (wavelength at 1.5405 Å) was carried out before and after the etching process via a PANalytical instrument at a current of 40 mA and a voltage of 40 kV. SEM micrographs were taken via an SEM Zeiss SUPRA 60 at 4 kV and a working distance of 3.5 mm.

Confocal spectral fluorescence imaging:

Confocal spectral fluorescence imaging was performed with an LSM 710 confocal microscope with a 34-channel Quasar detector (Zeiss, Oberkochen). The samples were excited with a 405 nm diode laser, and the emitted light was collected with an EC Plan-Neofluar 10x/0.30

objective. The microscope system was controlled, and images were acquired in λ mode with the ZEN black software version 2.3 SP1 FP3 (64-bit).

Acknowledgements

This project has received funding from the European Union's Horizon 2020 research and innovation programme under the Marie Skłodowska-Curie grant agreement PERSEPHONE (956270) and the project FOXES (951774), the German Research Foundation (DFG) through the project HIPER-LASE (441341044), and the German Ministry of Education and Research (BMBF) through the project NEPOMUQ (13N17112). This work was also supported by the Confocal Microscopy Facility, a Core Facility of the Interdisciplinary Center for Clinical Research (IZKF) Aachen within the Faculty of Medicine at RWTH Aachen University. The authors thank P. Grewe and Dr. U. Böttger (Electronic Material Research Lab, RWTH Aachen University) for their support in the XRD measurements. The author thanks Dr. V. Morad and Prof. Dr. M. Kovalenko (ETH Zurich) for providing the perovskite nanocrystals.

References

- [1] S. D. Stranks, G. E. Eperon, G. Grancini, C. Menelaou, M. J. P. Alcocer, T. Leijtens, L. M. Herz, A. Petrozza, H. J. Snaith, *Science* **2013**, *342*, 341.
- [2] M. Delor, A. H. Slavney, N. R. Wolf, M. R. Filip, J. B. Neaton, H. I. Karunadasa, N. S. Ginsberg, *ACS Energy Lett.* **2020**, *5*, 1337.
- [3] R. Xiao, Y. Hou, Y. Fu, X. Peng, Q. Wang, E. Gonzalez, S. Jin, D. Yu, *Nano Lett.* **2016**, *16*, 7710.
- [4] J. Lim, M. Kober-Czerny, Y.-H. Lin, J. M. Ball, N. Sakai, E. A. Duijnste, M. J. Hong, J. G. Labram, B. Wenger, H. J. Snaith, *Nat. Commun.* **2022**, *13*, 4201.
- [5] J. S. Manser, J. A. Christians, P. V. Kamat, *Chem. Rev.* **2016**, *116*, 12956.
- [6] S. X. Tao, X. Cao, P. A. Bobbert, *Sci. Rep.* **2017**, *7*, 14386.
- [7] Q. Ou, X. Bao, Y. Zhang, H. Shao, G. Xing, X. Li, L. Shao, Q. Bao, *Nano Mater. Sci.* **2019**, *1*, 268.
- [8] S. Liu, Y. Lu, C. Yu, J. Li, R. Luo, R. Guo, H. Liang, X. Jia, X. Guo, Y.-D. Wang, Q. Zhou, X. Wang, S. Yang, M. Sui, P. Müller-Buschbaum, Y. Hou, *Nature* **2024**, *1*.
- [9] M. A. Green, E. D. Dunlop, M. Yoshita, N. Kopidakis, K. Bothe, G. Siefer, X. Hao, *Prog. Photovolt. Res. Appl.* **2023**, *31*, 651.
- [10] K. O. Brinkmann, T. Becker, F. Zimmermann, C. Kreuzel, T. Gahlmann, M. Theisen, T. Haeger, S. Olthof, C. Tücmantel, M. Günster, T. Maschwitz, F. Göbelsmann, C. Koch, D. Hertel, P. Caprioglio, F. Peña-Camargo, L. Perdigón-Toro, A. Al-Ashouri, L. Merten, A. Hinderhofer, L. Gomell, S. Zhang, F. Schreiber, S. Albrecht, K. Meerholz, D. Neher, M. Stollerfoht, T. Riedl, *Nature* **2022**, *604*, 280.
- [11] Y. Wang, Y. Fan, X. Zhang, H. Tang, Q. Song, J. Han, S. Xiao, *ACS Nano* **2021**, *15*, 7386.
- [12] C. Huang, C. Zhang, S. Xiao, Y. Wang, Y. Fan, Y. Liu, N. Zhang, G. Qu, H. Ji, J. Han, L. Ge, Y. Kivshar, Q. Song, *Science* **2020**, *367*, 1018.
- [13] N. Pourdavoud, T. Haeger, A. Mayer, P. J. Cegielski, A. L. Giesecke, R. Heiderhoff, S. Olthof, S. Zaefferer, I. Shutsko, A. Henkel, D. Becker-Koch, M. Stein, M. Cehovski, O. Charfi, H.-H. Johannes, D. Rogalla, M. C. Lemme, M. Koch, Y. Vaynzof, K. Meerholz, W. Kowalsky, H.-C. Scheer, P. Görrn, T. Riedl, *Adv. Mater.* **2019**, *31*, 1903717.
- [14] W. Sun, Y. Liu, G. Qu, Y. Fan, W. Dai, Y. Wang, Q. Song, J. Han, S. Xiao, *Nat. Commun.* **2020**, *11*, 4862.
- [15] F. Yuan, G. Folpini, T. Liu, U. Singh, A. Treglia, J. W. M. Lim, J. Klarbring, S. I. Simak, I. A. Abrikosov, T. C. Sum, A. Petrozza, F. Gao, *Nat. Photonics* **2024**, *18*, 170.
- [16] K. Elkhoully, I. Goldberg, X. Zhang, N. Annavarapu, S. Hamdad, G. Croes, C. Rolin, J. Genoe, W. Qiu, R. Gehlhaar, P. Heremans, *Nat. Photonics* **2024**, *18*, 132.
- [17] H. Zhao, H. Chen, S. Bai, C. Kuang, X. Luo, P. Teng, C. Yin, P. Zeng, L. Hou, Y. Yang, L. Duan, F. Gao, M. Liu, *ACS Energy Lett.* **2021**, *6*, 2395.
- [18] X.-K. Liu, W. Xu, S. Bai, Y. Jin, J. Wang, R. H. Friend, F. Gao, *Nat. Mater.* **2021**, *20*, 10.
- [19] W. Bai, T. Xuan, H. Zhao, H. Dong, X. Cheng, L. Wang, R.-J. Xie, *Adv. Mater.* **2023**, *35*, 2302283.
- [20] R. L. Z. Hoye, J. Hidalgo, R. A. Jagt, J.-P. Correa-Baena, T. Fix, J. L. MacManus-Driscoll, *Adv. Energy Mater.* **2022**, *12*, 2100499.
- [21] M. R. Filip, G. E. Eperon, H. J. Snaith, F. Giustino, *Nat. Commun.* **2014**, *5*, 5757.
- [22] Q. A. Akkerman, V. D'Innocenzo, S. Accornero, A. Scarpellini, A. Petrozza, M. Prato, L. Manna, *J. Am. Chem. Soc.* **2015**, *137*, 10276.
- [23] X. Li, S. Aftab, S. Hussain, F. Kabir, A. M. A. Henaish, A. G. Al-Sehemi, M. R. Pallavolu, G. Koyyada, *J. Mater. Chem. A* **2024**, *12*, 4421.

- [24] L. Mao, C. C. Stoumpos, M. G. Kanatzidis, *J. Am. Chem. Soc.* **2019**, *141*, 1171.
- [25] Z. Yuan, C. Zhou, Y. Tian, Y. Shu, J. Messier, J. C. Wang, L. J. van de Burgt, K. Kountouriotis, Y. Xin, E. Holt, K. Schanze, R. Clark, T. Siegrist, B. Ma, *Nat. Commun.* **2017**, *8*, 14051.
- [26] R. F. Kahwagi, S. T. Thornton, B. Smith, G. I. Koleilat, *Front. Optoelectron.* **2020**, *13*, 196.
- [27] N. Calisi, E. Galvanetto, F. Borgioli, S. M. Martinuzzi, T. Bacci, S. Caporali, *Mater. Sci. Semicond. Process.* **2022**, *147*, 106721.
- [28] P. J. Cegielski, A. L. Giesecke, S. Neutzner, C. Porschatis, M. Gandini, D. Schall, C. A. R. Perini, J. Bolten, S. Suckow, S. Kataria, B. Chmielak, T. Wahlbrink, A. Petrozza, M. C. Lemme, *Nano Lett.* **2018**, *18*, 6915.
- [29] Z. Xu, X. Han, W. Wu, F. Li, R. Wang, H. Lu, Q. Lu, B. Ge, N. Cheng, X. Li, G. Yao, H. Hong, K. Liu, C. Pan, *Light Sci. Appl.* **2023**, *12*, 67.
- [30] P. Jastrzebska-Perfect, W. Zhu, M. Saravanapavanantham, Z. Li, S. O. Spector, R. Brenes, P. F. Satterthwaite, R. J. Ram, F. Niroui, *Nat. Commun.* **2023**, *14*, 3883.
- [31] Y. Liu, C. Gao, D. Li, X. Zhang, J. Zhu, M. Wu, W. Liu, T. Shi, X. He, J. Wang, H. Huang, Z. Sheng, D. Liang, X.-F. Yu, H. Zheng, X. Sun, Y. Ge, *Nat. Commun.* **2024**, *15*, 1588.
- [32] S. Deumel, A. van Breemen, G. Gelinck, B. Peeters, J. Maas, R. Verbeek, S. Shanmugam, H. Akkerman, E. Meulenkaamp, J. E. Huerdler, M. Acharya, M. García-Batlle, O. Almora, A. Guerrero, G. Garcia-Belmonte, W. Heiss, O. Schmidt, S. F. Tedde, *Nat. Electron.* **2021**, *4*, 681.
- [33] Y. Hou, J. Li, J. Yoon, A. M. Knoepfel, D. Yang, L. Zheng, T. Ye, S. Ghosh, S. Priya, K. Wang, *Sci. Adv.* **2023**, *9*, eade2338.
- [34] Y. Li, X. Jiang, Y. Chen, Y. Wang, Y. Wu, D. Yu, K. Wang, S. Bai, S. Xiao, Q. Song, *Light Sci. Appl.* **2023**, *12*, 184.
- [35] C. Soci, G. Adamo, D. Cortecchia, K. Wang, S. Xiao, Q. Song, A. L. Schall-Giesecke, P. J. Cegielski, M. C. Lemme, D. Gerace, D. Sanvitto, J. Tian, P. A. Tonkaev, S. V. Makarov, Y. S. Kivshar, O. A. Jimenez Gordillo, A. Melloni, A. P. Pushkarev, M. D'Amato, E. Lhuillier, A. Bramati, *Opt. Mater. X* **2023**, *17*, 100214.
- [36] S. Wu, Z. Chen, H.-L. Yip, A. K.-Y. Jen, *Matter* **2021**, *4*, 3814.
- [37] J. Bisquert, E. J. Juarez-Perez, *J. Phys. Chem. Lett.* **2019**, *10*, 5889.
- [38] Y.-H. Kye, C.-J. Yu, U.-G. Jong, Y. Chen, A. Walsh, *J. Phys. Chem. Lett.* **2018**, *9*, 2196.
- [39] J. Harwell, J. Burch, A. Fikouras, M. C. Gather, A. Di Falco, I. D. W. Samuel, *ACS Nano* **2019**, *13*, 3823.
- [40] A. Mayer, T. Haeger, M. Runkel, J. Staabs, J. Rond, F. van gen Hassend, P. Görrn, T. Riedl, H.-C. Scheer, *Appl. Phys. A* **2022**, *128*, 399.
- [41] L. A. Muscarella, A. Cordaro, G. Krause, D. Pal, G. Grimaldi, L. S. D. Antony, D. Langhorst, A. Callies, B. Bläsi, O. Höhn, A. F. Koenderink, A. Polman, B. Ehrler, *ACS Appl. Mater. Interfaces* **2022**, *14*, 38067.
- [42] X. He, P. Liu, H. Zhang, Q. Liao, J. Yao, H. Fu, *Adv. Mater.* **2017**, *29*, 1604510.
- [43] C. H. Lin, Q. Zeng, E. Lafalce, S. Yu, M. J. Smith, Y. J. Yoon, Y. Chang, Y. Jiang, Z. Lin, Z. V. Vardeny, V. V. Tsukruk, *Adv. Opt. Mater.* **2018**, *6*, 1800474.
- [44] M. S. Alias, Y. Yang, T. K. Ng, I. Dursun, D. Shi, M. I. Saidaminov, D. Priante, O. M. Bakr, B. S. Ooi, *J. Phys. Chem. Lett.* **2016**, *7*, 137.
- [45] M. Zhu, Y. Duan, N. Liu, H. Li, J. Li, P. Du, Z. Tan, G. Niu, L. Gao, Y. Huang, Z. Yin, J. Tang, *Adv. Funct. Mater.* **2019**, *29*, 1903294.
- [46] I. Shishkin, A. Polushkin, E. Tiguntseva, A. Murzin, B. Stroganov, Y. Kapitonov, S. A. Kulinich, A. Kuchmizhak, S. Makarov, *Appl. Phys. Express* **2019**, *12*, 122001.

- [47] J. Chen, Y. Wu, X. Li, F. Cao, Y. Gu, K. Liu, X. Liu, Y. Dong, J. Ji, H. Zeng, *Adv. Mater. Technol.* **2017**, *2*, 1700132.
- [48] J. Wu, J. Chen, Y. Zhang, Z. Xu, L. Zhao, T. Liu, D. Luo, W. Yang, K. Chen, Q. Hu, F. Ye, P. Wu, R. Zhu, Q. Gong, *Nano Lett.* **2017**, *17*, 3563.
- [49] W. Lee, J. Lee, H. Yun, J. Kim, J. Park, C. Choi, D. C. Kim, H. Seo, H. Lee, J. W. Yu, W. B. Lee, D.-H. Kim, *Adv. Mater.* **2017**, *29*, 1702902.
- [50] "Photoresist AZ MIR 701 Photoresists MicroChemicals GmbH," can be found under https://www.microchemicals.com/products/photoresists/az_mir_701.html, **n.d.**
- [51] N. Zhang, W. Sun, S. P. Rodrigues, K. Wang, Z. Gu, S. Wang, W. Cai, S. Xiao, Q. Song, *Adv. Mater.* **2017**, *29*, 1606205.
- [52] C. Zou, C. Chang, D. Sun, K. F. Böhringer, L. Y. Lin, *Nano Lett.* **2020**, *20*, 3710.
- [53] L. Nasi, D. Calestani, F. Mezzadri, F. Mariano, A. Listorti, P. Ferro, M. Mazzeo, R. Mosca, *Front. Chem.* **2020**, *8*, DOI 10.3389/fchem.2020.00313.
- [54] D. Xu, Q. Wan, S. Wu, Y. Zhao, X. Xu, L. Li, G. He, *RSC Adv.* **2020**, *10*, 17653.
- [55] L. Yang, D. Li, C. Wang, W. Yao, H. Wang, K. Huang, *J. Nanoparticle Res.* **2017**, *19*, 258.
- [56] A. L. Pellegrino, G. Malandrino, *ACS Appl. Energy Mater.* **2021**, *4*, 9431.
- [57] X. Tang, S. Han, Z. Zu, W. Hu, D. Zhou, J. Du, Z. Hu, S. Li, Z. Zang, *Front. Phys.* **2018**, *5*, DOI 10.3389/fphy.2017.00069.
- [58] M. Caputo, N. Cefarin, A. Radivo, N. Demitri, L. Gigli, J. R. Plaisier, M. Panighel, G. Di Santo, S. Moretti, A. Giglia, M. Polentarutti, F. De Angelis, E. Mosconi, P. Umari, M. Tormen, A. Goldoni, *Sci. Rep.* **2019**, *9*, 15159.
- [59] P. Fan, D. Gu, G.-X. Liang, J.-T. Luo, J.-L. Chen, Z.-H. Zheng, D.-P. Zhang, *Sci. Rep.* **2016**, *6*, 29910.
- [60] J. Li, Z. Han, J. Liu, Y. Zou, X. Xu, *Chem. Commun.* **2023**, *59*, 5156.
- [61] D. Solis-Ibarra, I. C. Smith, H. I. Karunadasa, *Chem. Sci.* **2015**, *6*, 4054.
- [62] H. Zhang, Q. Liao, X. Wang, K. Hu, J. Yao, H. Fu, *Small* **2016**, *12*, 3780.
- [63] H. Yue, D. Song, S. Zhao, Z. Xu, B. Qiao, S. Wu, J. Meng, *RSC Adv.* **2019**, *9*, 8373.
- [64] Laxmi, D. Kabra, *Adv. Photonics Res.* **2021**, *2*, 2000164.
- [65] D. Han, M. Imran, M. Zhang, S. Chang, X. Wu, X. Zhang, J. Tang, M. Wang, S. Ali, X. Li, G. Yu, J. Han, L. Wang, B. Zou, H. Zhong, *ACS Nano* **2018**, *12*, 8808.
- [66] N. Jarmouni, M. Tomaiuolo, A. Gabbani, D. Genovese, F. Pineider, R. Bassam, S. Belaouad, S. Benmokhtar, *Mater. Today Proc.* **2022**, *58*, 1480.
- [67] X. Li, Z. Xue, D. Luo, C. Huang, L. Liu, X. Qiao, C. Liu, Q. Song, C. Yan, Y. Li, T. Wang, *Sci. China Mater.* **2018**, *61*, 363.
- [68] L. Protesescu, S. Yakunin, M. I. Bodnarchuk, F. Bertolotti, N. Masciocchi, A. Guagliardi, M. V. Kovalenko, *J. Am. Chem. Soc.* **2016**, *138*, 14202.

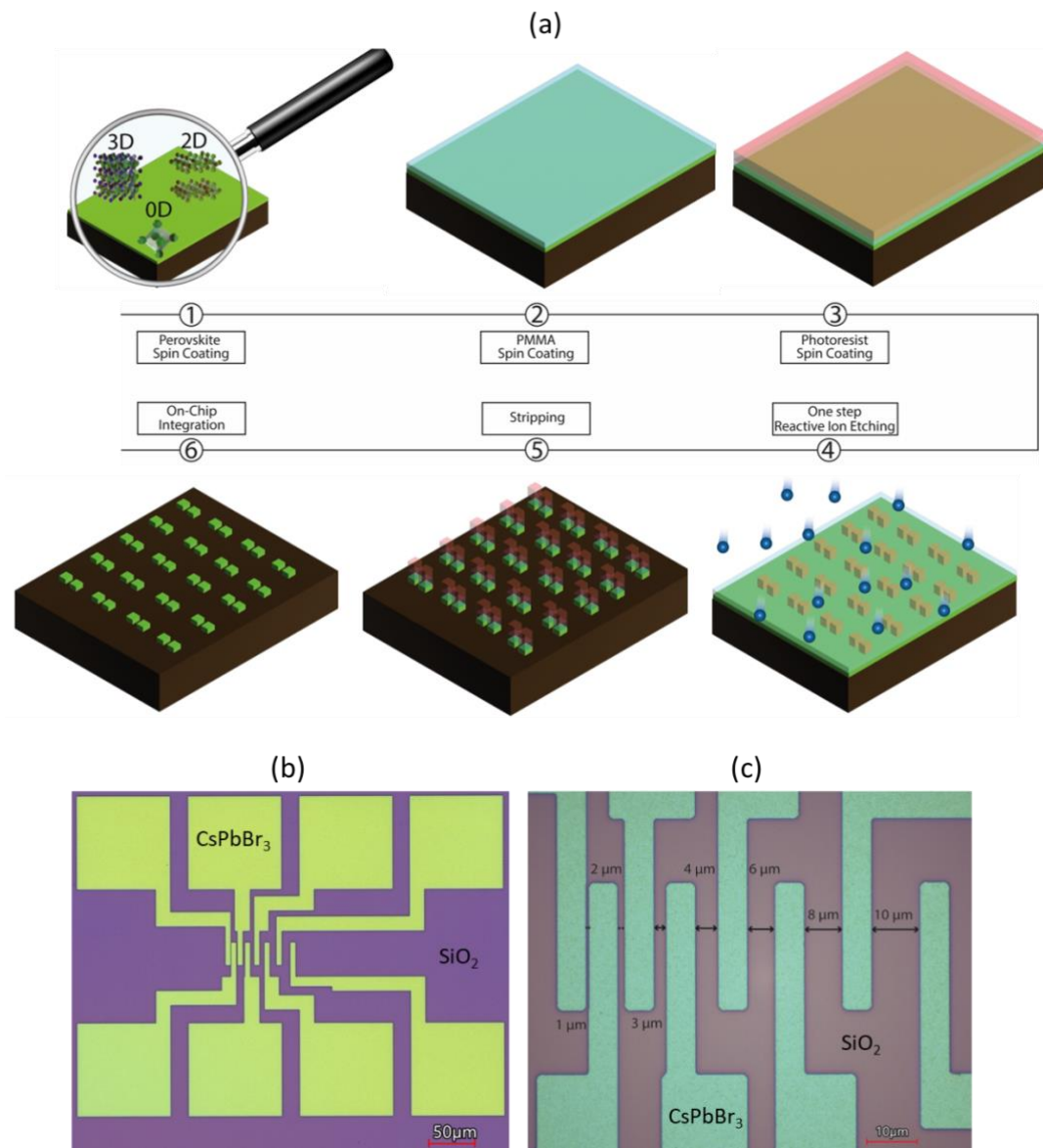


Figure 1. (a) The fabrication process includes the following steps: (1) Deposition of the perovskite thin film (3D, 2D or 0D), (2) Deposition of the PMMA layer, (3) Deposition of the top photoactive resist layer (AZ MIR 701), (4) Development of the AZ MIR 701 resist layer and pattern transfer into the perovskite layer by reactive ion etching, (5) Stripping by dissolving the bottom resist layer and lifting the top layer, and (6) Top-down patterned perovskite devices. (b)-(c) Optical microscope image of device features achieved by top-down patterning method with a minimum feature dimension of 1 μm.

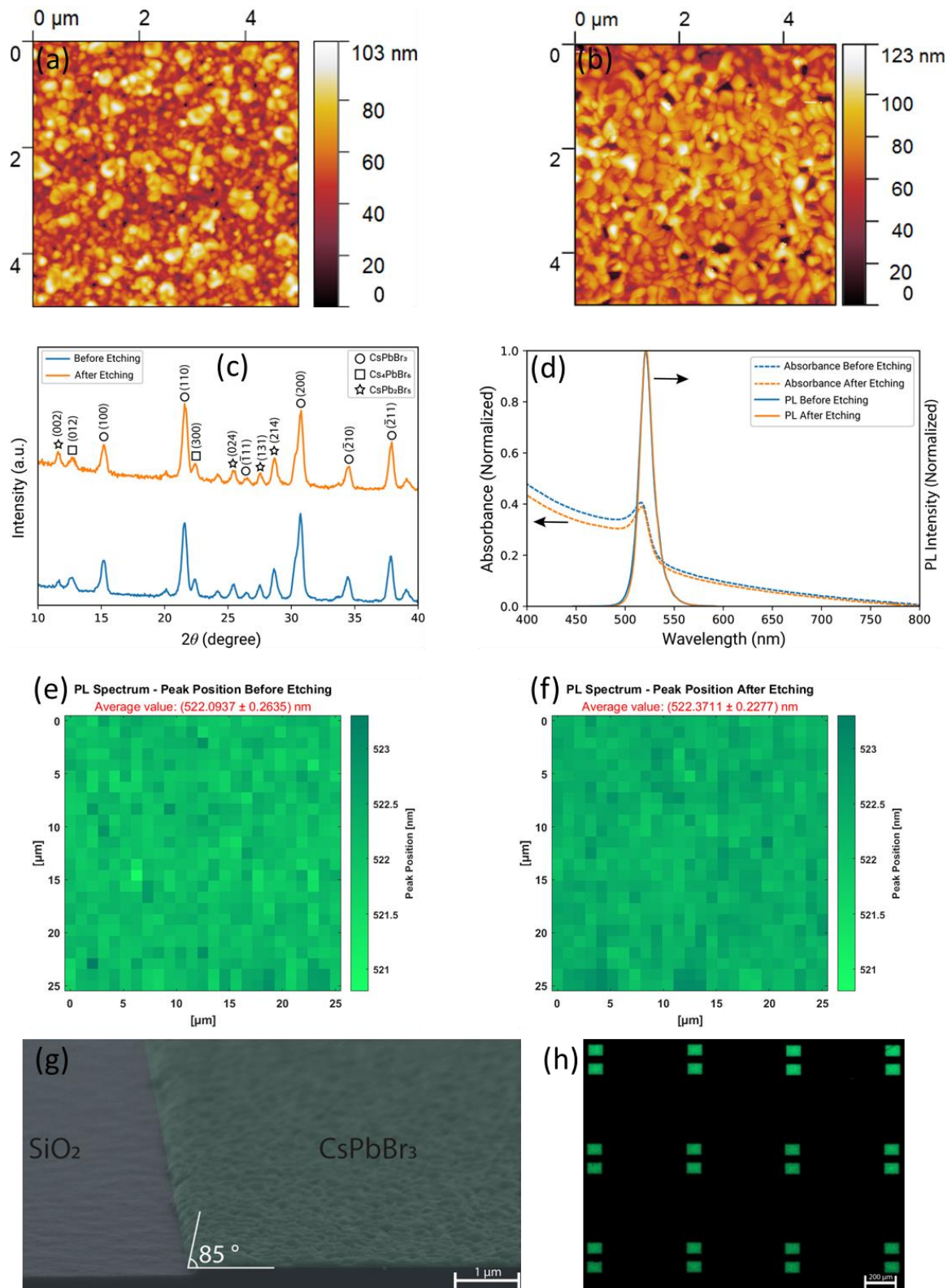


Figure 2. CsPbBr₃ patterning. (a) AFM scan of the pristine sample. (b) AFM scan after etching and stripping of the double stack. (c) X-ray diffraction patterns of the samples before and after etching. (d) UV–Vis spectra and PL spectra before and after etching. (e) – (f) Comparison of PL peak positions before and after etching over an area of 25 μm × 25 μm. (g) Cross-sectional SEM image of the etched structure. (h) Confocal fluorescence microscope image of an array of etched structures.

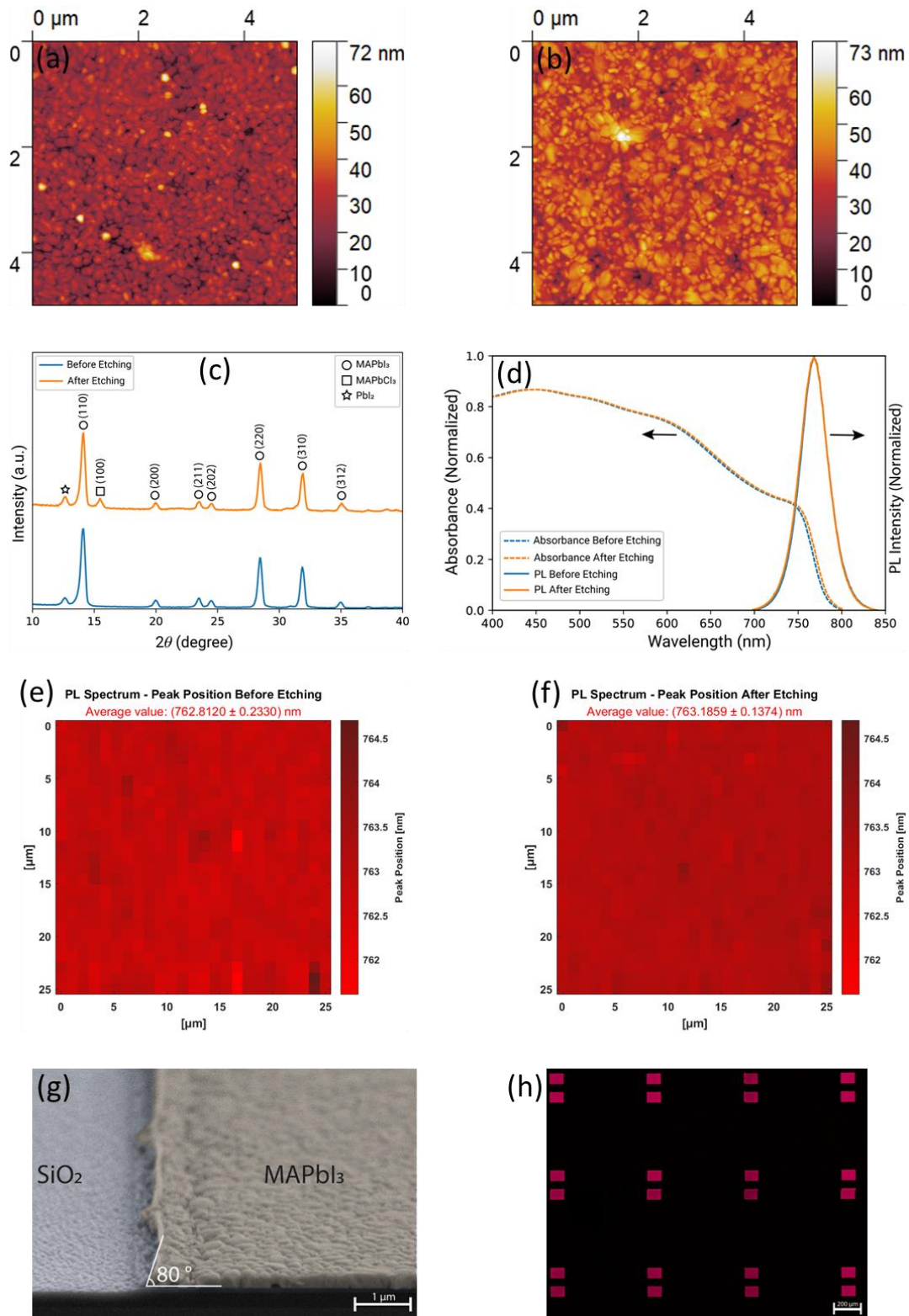


Figure 3. MAPbI₃ patterning. (a) AFM scan of the pristine sample. (b) AFM scan after etching and stripping of the double stack. (c) X-ray diffraction patterns of the samples before and after etching. (d) UV–Vis spectra and PL spectra before and after etching. (e) – (f) Comparison of PL peak positions before and after etching over an area of 25 μm × 25 μm. (g) Cross-sectional SEM image of the etched structure. (h) Confocal fluorescence microscope image of an array of etched structures.

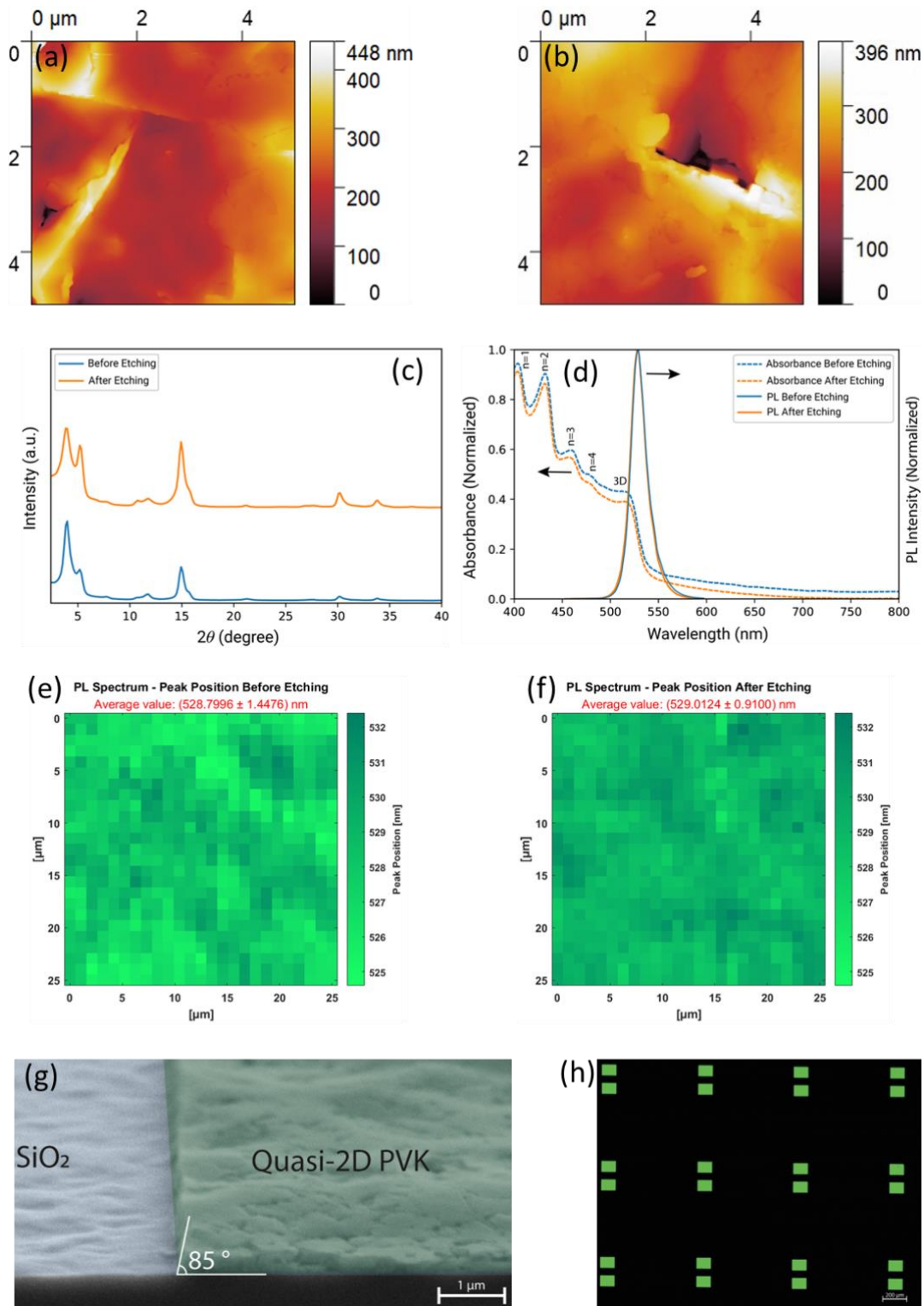


Figure 4. $\text{PEA}_2(\text{MAPbBr}_3)_{n-1}\text{PbBr}_4$ quasi-2D perovskite patterning. (a) AFM scan of the pristine sample. (b) AFM scan after etching and stripping of the double stack. (c) X-ray diffraction patterns of the samples before and after etching. (d) UV-Vis spectra and PL spectra before and after etching. (e) – (f) Comparison of PL peak positions before and after etching over an area of $25 \mu\text{m} \times 25 \mu\text{m}$. (g) Cross-sectional SEM image of the etched structure. (h) Confocal fluorescence microscope image of an array of etched structures.

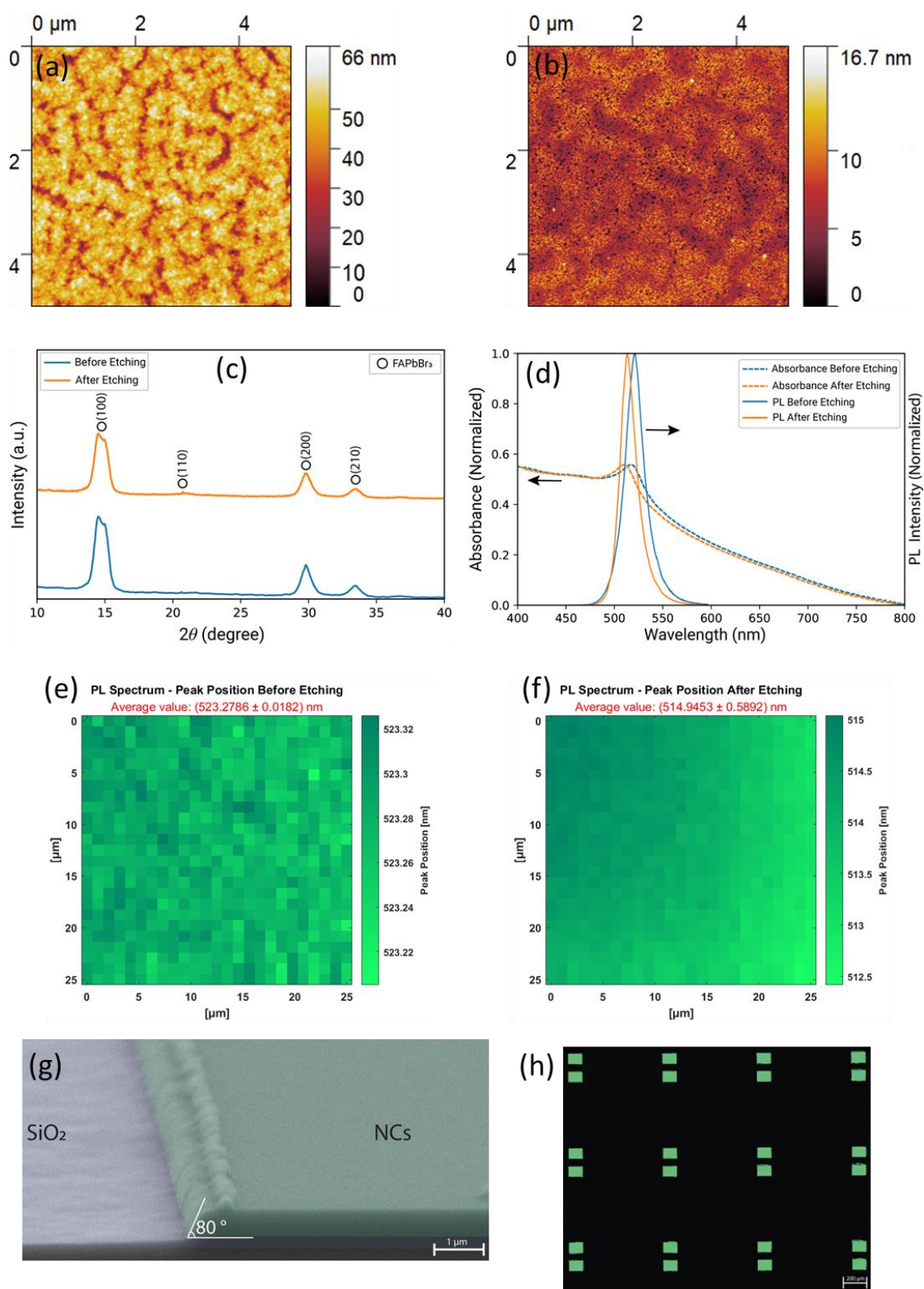


Figure 5. FAPbBr₃ patterning. (a) AFM scan map of the pristine sample. (b) AFM scan map after etching and stripping of the double stack. (c) X-ray diffraction patterns of the samples before and after etching. (d) UV–Vis spectra and PL spectra before and after etching. (e) – (f) Comparison of PL peak positions before and after etching over an area of 25 μm × 25 μm. (g) Cross-sectional SEM image of the etched structure. (h) Confocal fluorescence microscope image of an array of etched structures.

SUPPLEMENTARY INFORMATION

Versatile Top-Down Patterning of 3D, 2D and 0D Perovskites for On-Chip Integration

Federico Fabrizi^{1,2,°}, Saeed Goudarzi^{2,°}, Sana Khan^{1,2}, Tauheed Mohammad¹, Liudmila Starodubtceva², Piotr J. Cegielski¹, Gerhard Müller-Newen³, Surendra B. Anantharaman^{1,4}, Maryam Mohammadi^{1,}, Max C. Lemme^{1,2,*}*

¹AMO GmbH, Otto-Blumenthal-Straße 25, Aachen, Germany.

²Chair of Electronic Devices, RWTH Aachen University, Otto-Blumenthal-Straße 25, Aachen, Germany.

³Institute of Biochemistry and Molecular Biology, Uniklinik RWTH Aachen, Pauwelsstrasse 30, Aachen, Germany.

⁴Low-dimensional Semiconductors (LDS) Lab, Indian Institute of Technology Madras, Chennai, Tamil Nadu, India.

[°]These authors contributed equally.

*Corresponding Authors – mohammadi@amo.de, lemme@amo.de

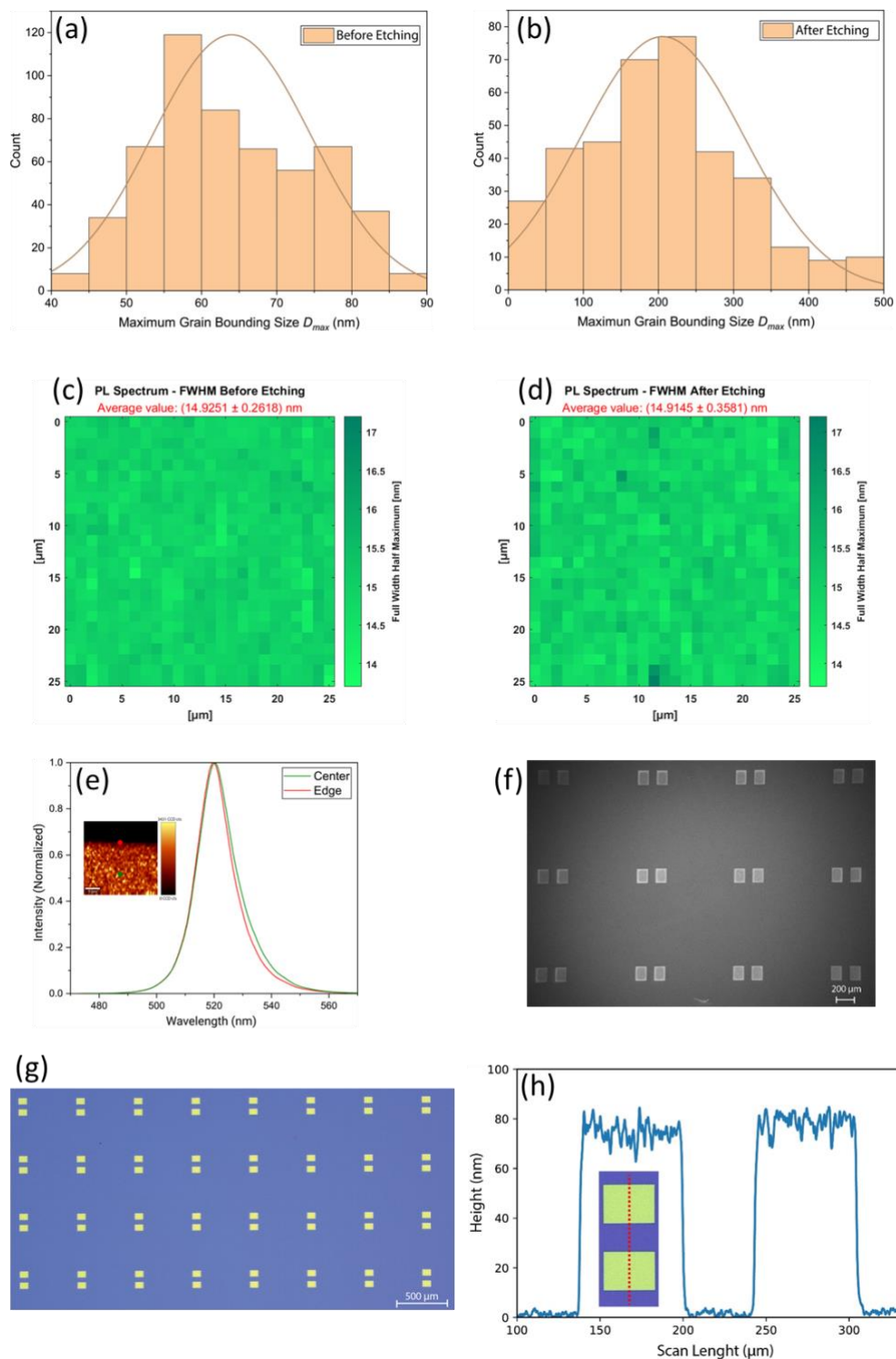
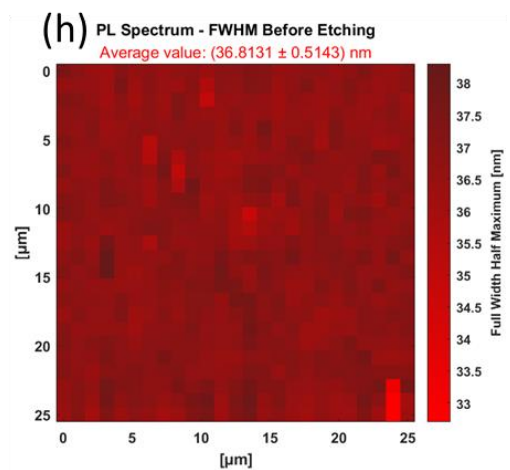
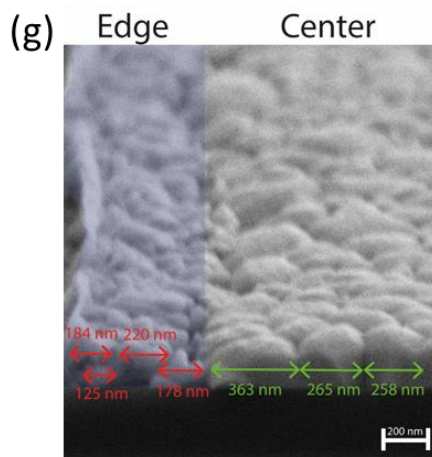
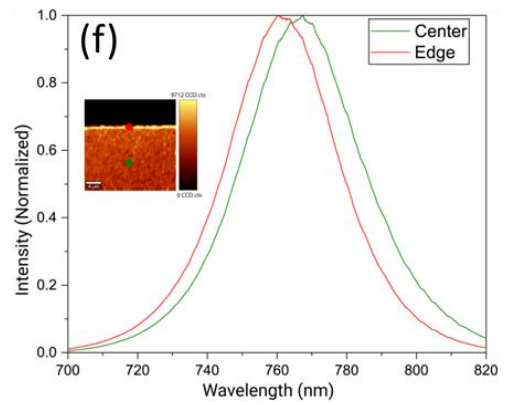
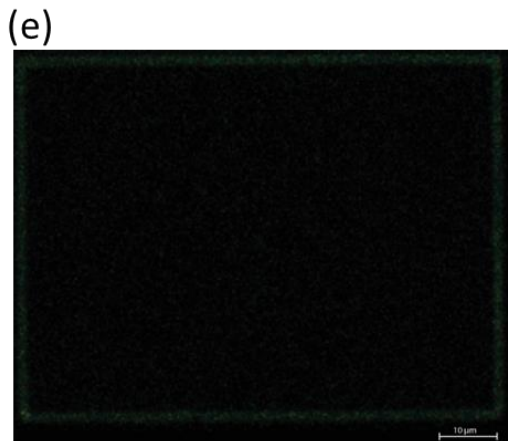
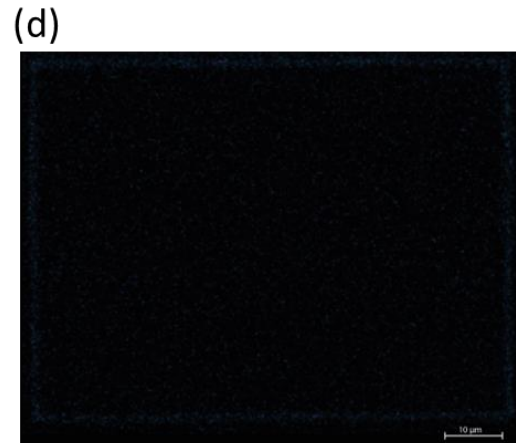
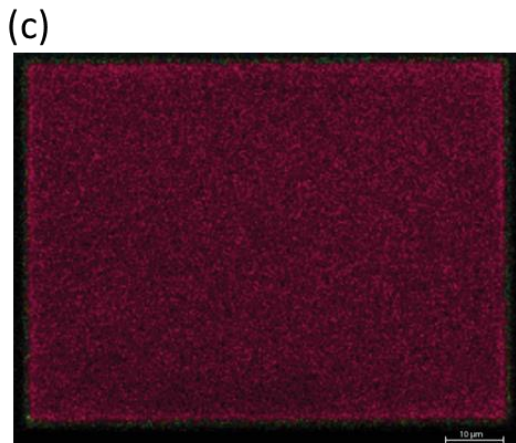
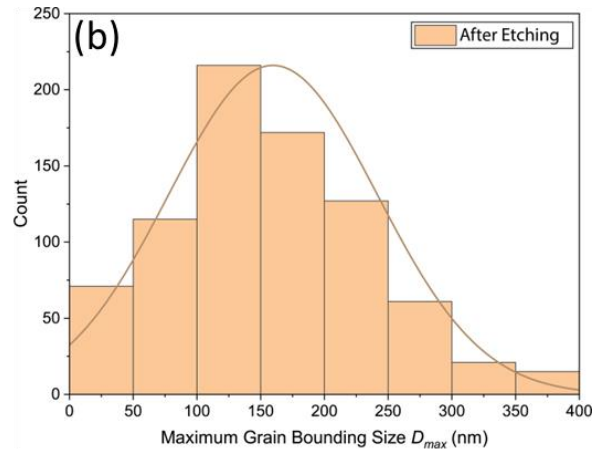
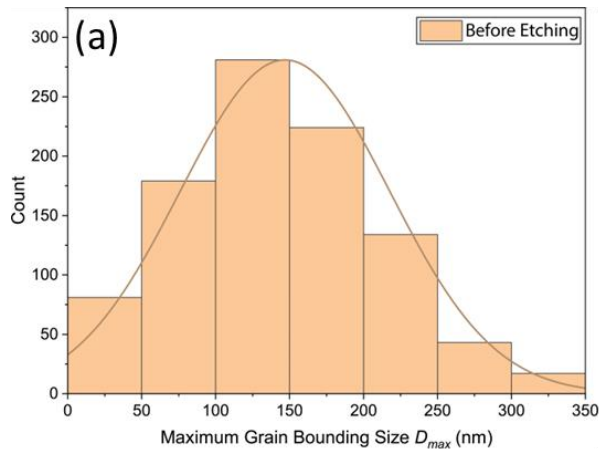


Figure S1. CsPbBr₃ patterning supplementary information. (a)-(b) Histogram plots of the grain size distribution before and after the etching process. (c)-(d) Large area scans of 25 μ m x 25 μ m before and after etching, where each pixel corresponds to a fitted value of the FWHM of the PL spectrum. (e) PL spectrum comparison between the edge and center of the etched structure. (f) Top-view SEM image. (g) Optical microscope image of the patterned structures. (h) Surface profilometer line scan of the etched structures after the stripping of the photoresist.



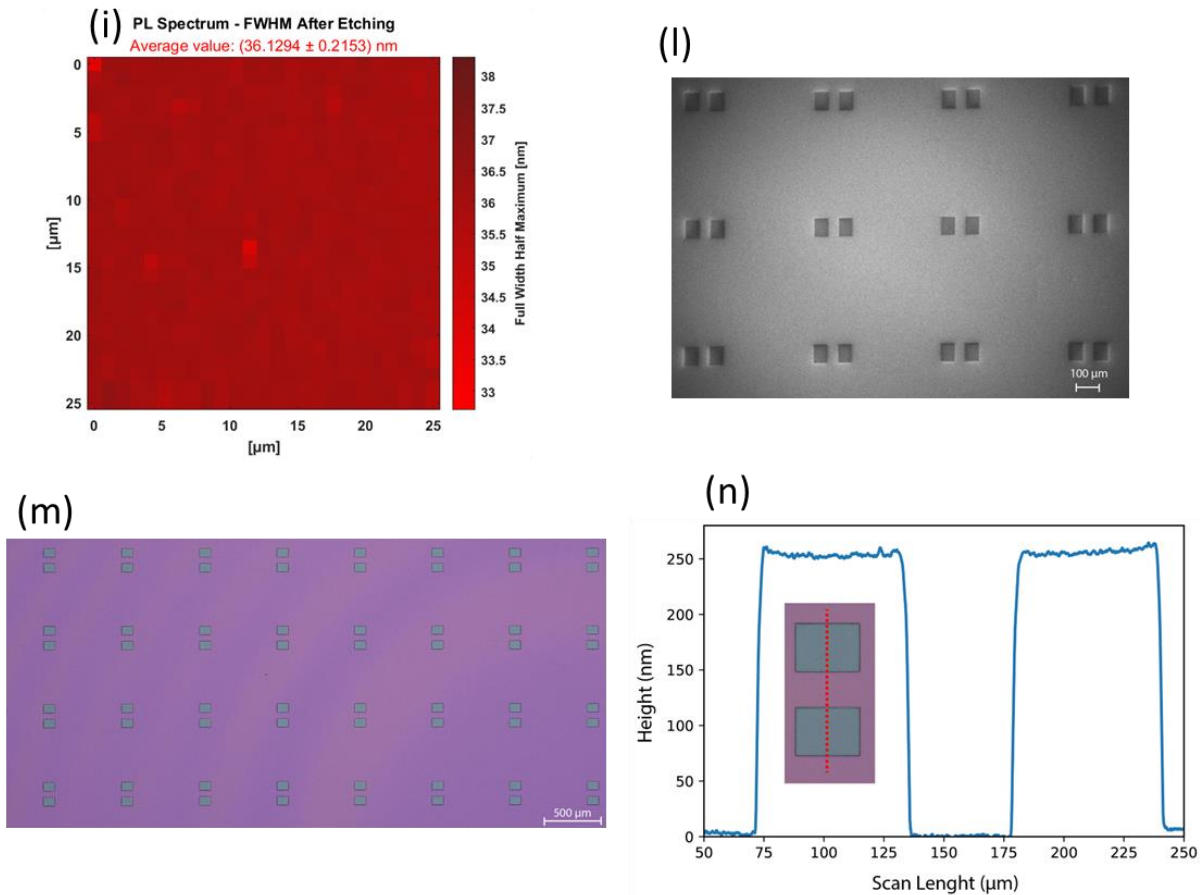


Figure S2. MAPbI₃ patterning supplementary information. (a)-(b) Histogram plots of the grain size distribution before and after the etching process. (c) Confocal image of one etched structure. A blue/green shallowness around the edges is visible. This is a confirmation of the local doping of the MAPbI₃ due to the etching gases used during the process. (d)-(e) Green and blue emission components coming from a mixed halide phase forming during the process. (f) PL spectrum comparison between the edge and center of the etched structure. A clear blue shift in the PL peak position on the edge is visible. (g) SEM cross-section image, where is visible a clear reduction in the grain sizes between the edge and the center of the etched area. (h)-(i) Large are scans of 25 μm x 25 μm before and after etching. Each pixel corresponds to a fitted value of the FWHM of the PL spectrum. (l) Top-view SEM image. (m) Optical microscope image of the patterned structures. (n) Surface profilometer line scan of the etched structures after the stripping of the photoresist.

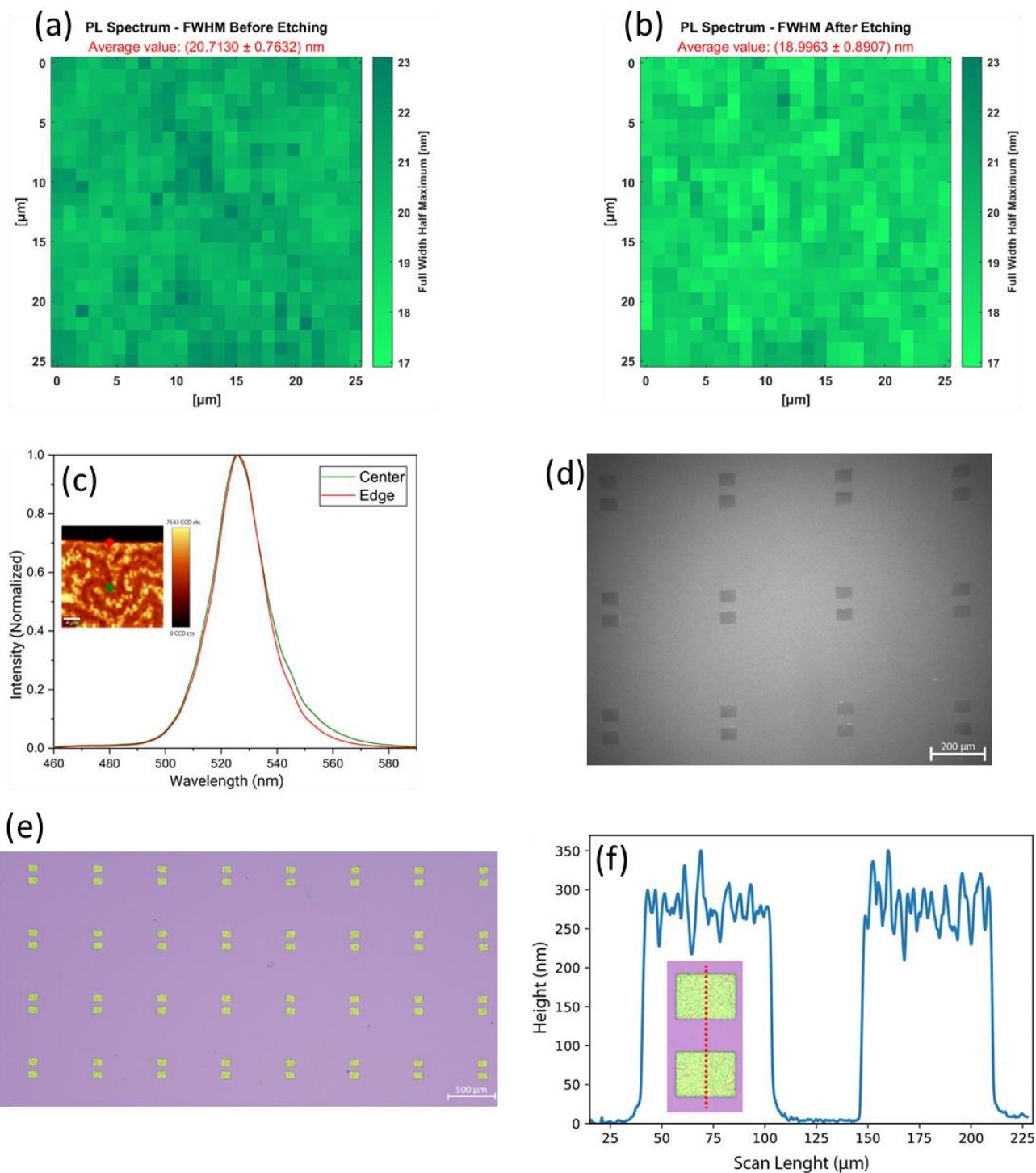


Figure S3. $\text{PEA}_2(\text{MAPbBr}_3)_{n-1}\text{PbBr}_4$ quasi-2D patterning supplementary information. (a)-(b) Large are scans of 25 μm x 25 μm before and after etching, where each pixel corresponds to a fitted value of the FWHM of the PL spectrum. (c) PL spectrum comparison between the edge and center of the etched structure. (d) Top-view SEM image. (f) Optical microscope image of the patterned structures. (g) Surface profilometer scan line of the etched structures after the stripping of the photoresist.

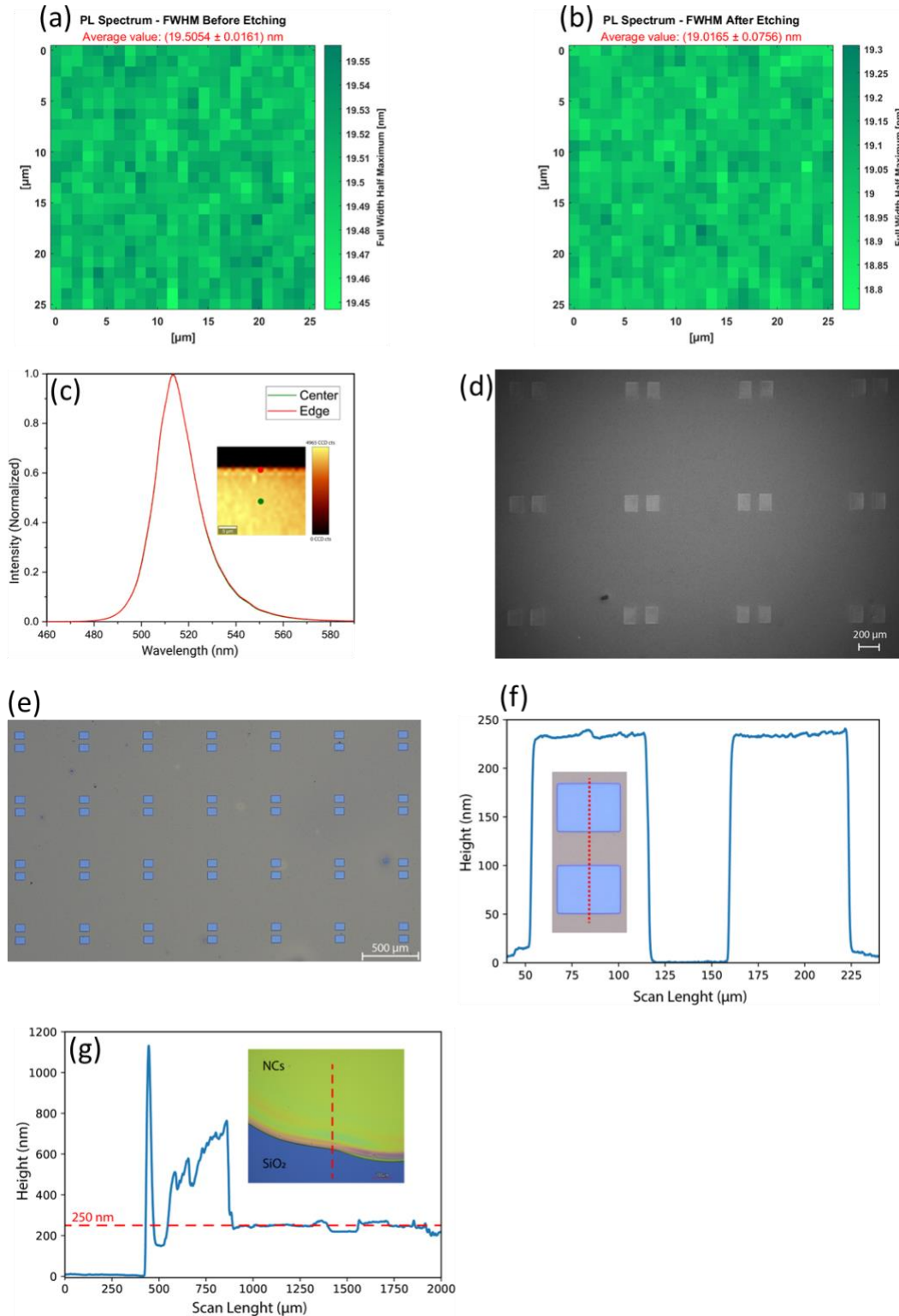


Figure S4. FAPbBr₃ NCs patterning supplementary information. (a)-(b) Large are scans of 25 μm x 25 μm before and after etching, where each pixel corresponds to a fitted value of the FWHM of the PL spectrum. (c) PL spectrum comparison between the edge and center of the etched structure. (d) Top-view SEM image. (e) Optical microscope image of the patterned structures. (f) Surface profilometer scan line of the etched structures after the stripping of the photoresist. (g) Surface profilometer scan line of the etched structures after the spin coating and before the nanofabrication process.